ARTICLE

Guided Assembly of Gold Colloidal Nanoparticles on Silicon Substrates Prepatterned by Charged Particle Beams

Miroslav Kolíbal,[†,‡,*] Martin Konečný,[†] Filip Ligmajer,[†] David Škoda,[†,‡] Tomáš Vystavěl,[§] Jakub Zlámal,[†,‡] Peter Varga,[‡,⊥] and Tomáš Šikola[†,‡]

[†]Institute of Physical Engineering, Brno University of Technology, Technická 2, 616 69 Brno, Czech Republic, [‡]CEITEC BUT, Brno University of Technology, Technická 10, 616 69 Brno, Czech Republic, [§]FEI Company, Podnikatelská 6, 612 00 Brno, Czech Republic, and [⊥]Institut für Angewandte Physik, Technische Universität Wien, A-1040 Wien, Austria

ABSTRACT

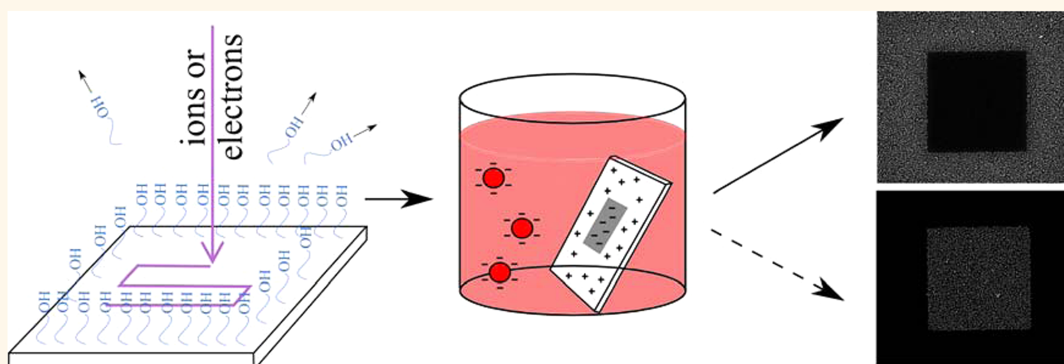

Colloidal gold nanoparticles represent technological building blocks which are easy to fabricate while keeping full control of their shape and dimensions. Here, we report on a simple two-step maskless process to assemble gold nanoparticles from a water colloidal solution at specific sites of a silicon surface. First, the silicon substrate covered by native oxide is exposed to a charged particle beam (ions or electrons) and then immersed in a HF-modified solution of colloidal nanoparticles. The irradiation of the native oxide layer by a low-fluence charged particle beam causes changes in the type of surface-terminating groups, while the large fluences induce even more profound modification of surface composition. Hence, by a proper selection of the initial substrate termination, solution pH, and beam fluence, either positive or negative deposition of the colloidal nanoparticles can be achieved.

KEYWORDS: nanoparticle adhesion · nanofabrication · dual beam · FIB · silicon · gold · self-assembly · selective growth · guided growth · surface potential

Gold nanoparticle arrays are utilized in vapor–liquid–solid growth of nanowires,[1,2] where the interface between the liquid eutectic droplet and the substrate acts as a preferential nucleation site, resulting in vertical nanowire growth with the eutectic droplet on top of nanowires.[3] In a reversed process, called metal-assisted chemical etching, selective etchants are used to remove the material just below the nanoparticle, thus forming nanopores or nanocolumn arrays.[4,5] Obviously, nanoparticle dimensions (which directly determine the nanowire/nanopore diameter) and position on the substrate are critical for further processing and utilization. Additionally, metallic nanoparticles are an intensively studied subject in the field of plasmonics.[6,7] For example, a linear chain of nanoparticles (*e.g.*, gold or silver) acts as a plasmonic waveguide,[8−10] where the subwavelength light transmission is dependent on the nanoparticle size and interparticle distance. Moreover, such a linear chain can be utilized as a contact electrode.[11]

Although the metallic particles of different sizes are commercially available in colloidal solution, a significant issue is to place

* Address correspondence to kolibal.m@fme.vutbr.cz.

Received for review August 21, 2012 and accepted October 21, 2012.

Published online October 25, 2012
10.1021/nn3038226

© 2012 American Chemical Society

them onto a desired substrate site-selectively. Two main approaches have been developed until now: chemical recognition and electrostatic force attraction of nanoparticles. Considering the chemical recognition technique, the gold nanoparticles are usually bound to thiolated DNA patterned by the means of electron beam lithography.[1,12−15] The latter method utilizes the fact that the colloidal particles bear a negative or positive charge due to the presence of carboxylate or amine end groups in the nanoparticle organic shell. To bind the particles to specific substrate sites, the surface should be electrically charged either by a positively charged polymer layer[16−22] or by a direct injection of an electrical charge into a charge-trapping layer (electret).[23−27]

For certain applications the presence of an interfacial layer between the metal nanoparticle and the substrate is detrimental. In nanowire growth, the thin polymer layer residues may cause different nanowire growth orientation and hinder the crystalline growth.[28] In another example, the plasmonic resonant frequency of metal nanoparticles is strongly affected by the close dielectric surroundings,[29] and hence, the processing layer would shift the surface plasmon resonances from the desired ones. Therefore, an intensive effort has been made to find a technique in which the interfacial layer would be avoided. Direct patterning of insulating substrates by charged particle beams was demonstrated employing both ion and electron beams.[30−33] However, the reported resolution is on a micrometer scale, and inherently, the techniques presented so far cannot be applied to pattern semi- or conductive samples. Additionally, the ambiguous insight into the patterning principles by particle beams is still prevailing. Too much attention has been paid to the charge polarity (ions or electrons) of the beams used for initiation of the guided growth of the charged colloidal particles. Here we demonstrate that the application of both ions and electrons can lead to similar results in the formation of patterns capable of attracting (positive deposition) or repelling (negative deposition) negatively charged Au colloidal particles. In contrast to generally accepted explanation, we show that the incoming beams alter the surface chemistry rather than provide subsurface charging. The technique can thus be also applied to semi- or conductive substrates using 2 orders of magnitude lower fluences ($\approx 10^{13}$–10^{14} cm^{-2}) than conventional ion beam etching or deposition ($\geq 10^{16}$ cm^{-2}), allowing the placement of a single isolated nanoparticle with precision of several nanometers.

Our two-step process provides both positive and negative deposition of patterns of gold nanoparticles. The key factor in the selective particle−substrate interaction is an interplay between the integral modifications of surface-terminating groups by changing the pH of the colloidal solution and the local changes of the end groups at specific sample sites by their exposure to focused ion or electron beams. To demonstrate the technique, we have chosen a simple system consisting of silicon substrates covered with native oxide and negatively charged 20 nm spherical gold nanoparticles (without any additional electret or polymer layers). First, we will discuss the adhesion of gold nanoparticles on a silicon substrate surface without beam patterning. Then we will show how the beam irradiation affects the nanoparticle adhesion and finally give examples of guided positive or negative deposition of the nanoparticles from a colloidal solution to specific sites of patterned samples.

Adhesion on a Bare Substrate. In Figure 1a, the zeta (surface) potential of two distinct silicon substrates with native oxide dipped in the colloidal solutions having different pH is schematically shown. The as-received 20 nm gold colloidal solution has a pH of 5.5, which is above the isoelectric point of any silicon wafer.[34] The adhesion of gold nanoparticles from the as-received solution is therefore efficiently prevented (image I in Figure 1a) due to the repulsion between the two negatively charged surfaces ($-COO^-$ termination of Au colloidal nanoparticles and $-O^-$ termination of the native oxide). To attract colloidal nanoparticles, the solution has to be acidified below the isoelectric point, turning the surface potential of the substrate to positive values.[35−37] The acidification of the colloidal solution results also in partial neutralization of $-COO^-$ termination (formation of $-COOH$) of Au colloidal nanoparticles, and hence, careless increasing of the HF concentration would be detrimental to the stability of the colloidal solution (aggregation of the nanoparticles due to van der Waals forces).

Both studied substrates are covered with the native oxide of similar thickness (proved by XPS); however, due to distinct final wafer fabrication procedures (see Methods), the surfaces are terminated in a different way. The first sample, denoted as sample A, is initially more hydrophobic due to the additional presence of $-H$[38] and $Si-O-CH_x$ end groups (see Supporting Information, Figure S1), and sample B is hydrophilic due to a majority of $Si-OH$ end groups.[38] These end groups determine the surface potential because they can be ionized *via* protonation (formation of $-OH_2^+$ at low pH)[35−37] or deprotonation (formation of $-O^-$ at higher pH)[37] events in solutions with different pH. The analysis of the oxygen peak in XPS spectra of both samples reveals the distinct character of surface termination. The O 1s and the oxide-related component of the Si 2p peaks are shifted toward higher binding energies in the case of sample B (see Figure 1b,c). The shift is associated with the higher concentration of positively charged species ($-OH_2^+$) on the surface of sample B.[37] The difference in sample properties is demonstrated by the experiments on deposition of 20 nm gold nanoparticles (see Figure 1a). As the isoelectric point is

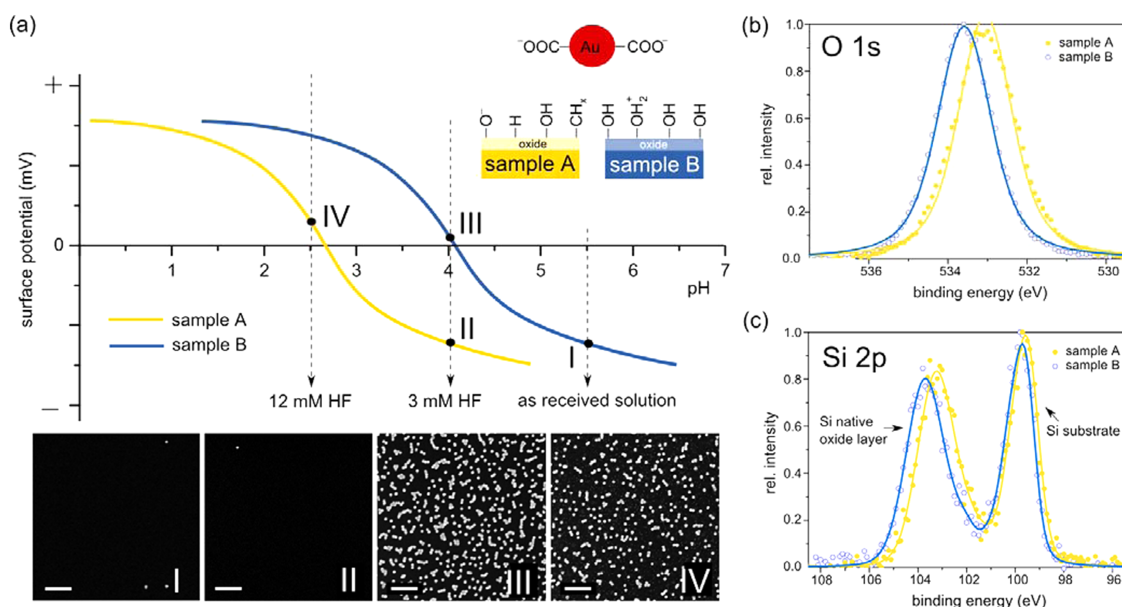

Figure 1. Adhesion on bare Si substrates. (a) Schematic representation of the surface potential of silicon wafers with two distinct isoelectric points. The images below show the Au nanoparticles' coverage on the sample surface after its 2 h immersion in as-received colloidal solution (sample B, image I) and in the 3 mM HF-modified colloidal solution (sample A, image II, and sample B, image III). Image IV shows sample A after its 2 h immersion in the 12 mM HF-modified colloidal solution. Scale bars, 200 nm. (b) O 1s peak in XPS spectra of pristine samples. A shift of ~0.4 eV toward higher binding energy with respect to sample A is observed for sample B. (c) Similar shift is also observed for the oxide-related component of the Si 2p peak for sample B.

above pH 2.5 and 4 for samples A and B, respectively, to deposit the colloidal nanoparticles on sample A (*i.e.*, to change the polarity of the surface potential), the pH of the as-received colloidal solution (originally pH 5.5) has to be lowered more than for the sample B (12 mM HF concentration; see Figure 1a). Higher concentration of HF causes dissolution of the initial surface termination (–H and $-CH_x$ terminating groups) due to the pronounced oxide etching (Supporting Information, Figure S1). Since the surface is being simultaneously slightly reoxidized during etching due to the presence of dissolved oxygen in solution, a thin oxide layer is still present, however, this time terminated by the –OH and $-OH_2^+$ groups.[38] The exchange of the surface end groups is accompanied by turning sample A hydrophilic, similarly to the sample B, and the positive surface potential allows the deposition of negatively charged nanoparticles (see image IV in Figure 1a). The difference in isoelectric points of the two substrates facilitates the positive and negative deposition, as will be shown below.

Adhesion on Ion-Beam-Modified Surfaces. To observe the effect of the exposure of both types of substrates to charged particle beams, their local modification by a Ga^+ focused ion beam (FIB) was carried out. An array of $3 \times 3\ \mu m^2$ squares was prepared using different doses of 5 keV ions and subsequently immersed in the 3 mM HF-modified colloidal solution. The results of the nanoparticle deposition are shown in Figure 2a–d. In agreement with the data presented in Figure 1, the nanoparticles adhered to an ion-untreated surface only in the case of sample B (Figure 2b,d, outside the exposed square). However, the area irradiated by a low ion fluence (1×10^{14} cm^{-2}) shows even higher nanoparticle concentration than the surrounding surface of this sample (see the nanoparticle concentration data in Figure 2e). In the case of sample A, the nanoparticles adhered properly to the area irradiated by the low fluence of the ion beam only (Figure 2a). The XPS analysis has shown that the O 1s peak for sample A is slightly shifted toward higher binding energy after FIB irradiation (see Figure 2g). With the ion fluence increasing above 1×10^{14} cm^{-2}, the density of the deposited nanoparticles on irradiated areas decreases and the nanoparticle adhesion is completely suppressed for fluences higher than 8×10^{14} and 1×10^{15} cm^{-2} for samples A and B, respectively (Figure 2c,d). In Figure 2c, there is an apparent rim around the patterned square on sample A with an enhanced nanoparticle adhesion, which is caused by irradiation of the area surrounding the desired pattern by lower fluences of ions in the beam tail of the nongaussian beam.[39] The XPS data show a build up of a contamination layer after the prolonged exposure (see Supporting Information, Figure S2) and, also, a shift of the O 1s peak back to the lower binding energy. A detailed analysis of the SEM images is shown in Figure 2e, where the dependence of the nanoparticle concentration (as calculated from the SEM images, see Methods) on the ion fluence is presented. The horizontal line marks the concentration of the particles on an unexposed surface of sample B. In addition, we also show the data taken on sample B

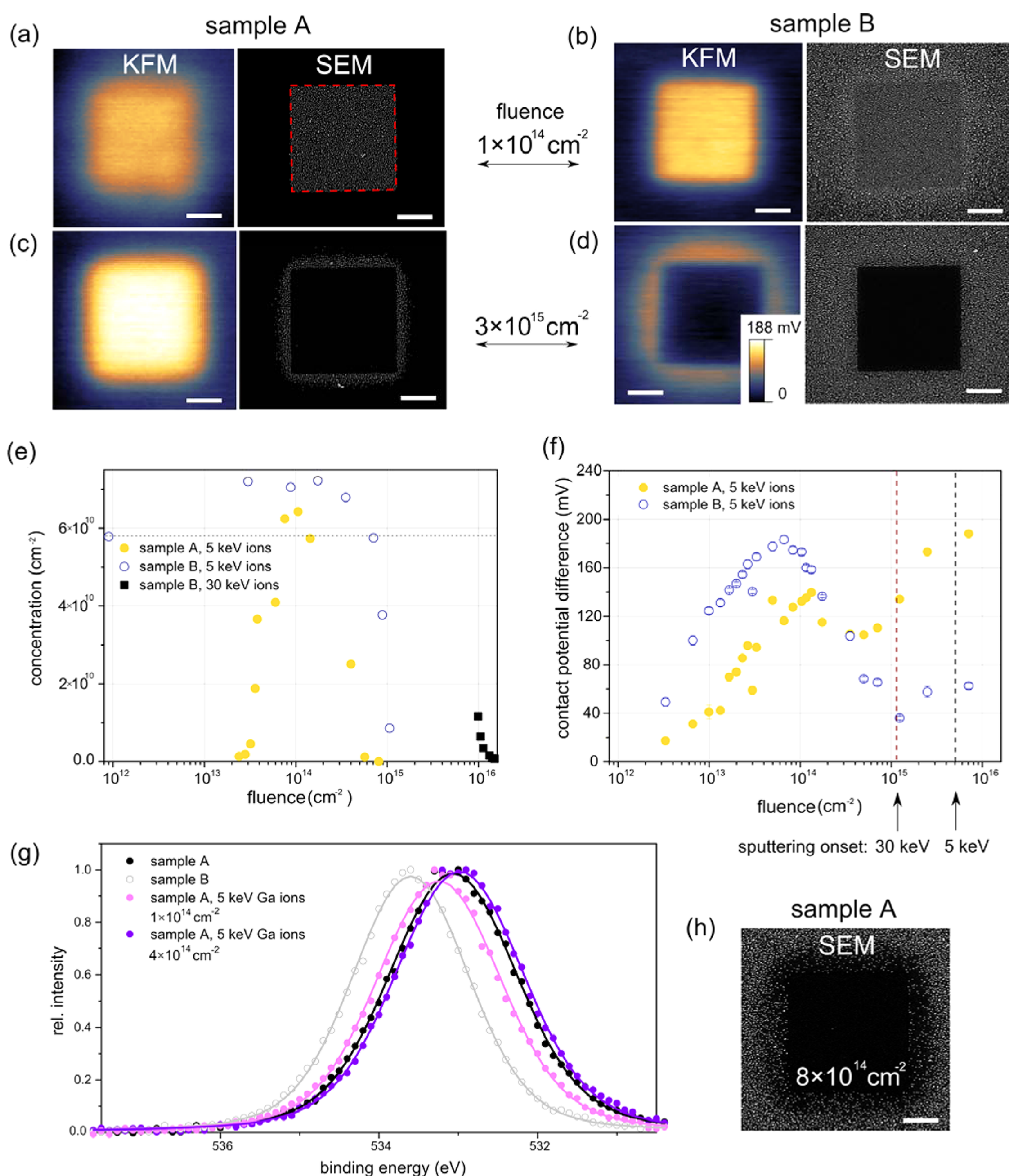

Figure 2. Depositon of gold nanoparticles from the colloidal solution on the beam-exposed areas. (a–d) KFM images (left) of patterned substrates after ion irradiation and SEM images (right) after subsequent immersion in the 3 mM HF-modified Au colloidal solution: sample A (a,c) and sample B (b,d). Patterning was done by 5 keV ions with a fluence of 1×10^{14} cm^{-2} (a,b) and 3×10^{15} cm^{-2} (c,d). The dimensions of the square patterns are 3×3 μm^2 (as marked by the dashed red line in (a)). Due to low magnification of the images, the individual nanoparticles cannot be resolved, but their presence is indicated by the brighter areas (gray). (e) Au nanoparticle surface concentration (as counted from SEM images) as a function of ion fluence. The horizontal line represents their concentration on the unexposed sample B (for sample A, this concentration is zero). (f) Contact potential difference (measured by KFM) as a function of ion fluence for 5 keV Ga$^+$ ions. The vertical dashed lines mark the sputtering onsets for 5 keV (5×10^{15} cm^{-2}) and 30 keV (1×10^{15} cm^{-2}) ions. (g) O 1s peak measured by XPS on sample A irradiated by FIB. A shift toward higher binding energy is observed for 1×10^{14} cm^{-2} fluence, corresponding to the concentration maximum in (e). For a larger fluence (4×10^{14} cm^{-2}), a shift toward lower binding energy is detected. O 1s peaks associated with the pristine samples A (filled circles) and B (open circles) are shown for comparison. (h) SEM image of the patterned sample A (fluence 8×10^{14} cm^{-2}) after its immersion in the 12 mM HF-modified Au colloidal solution. Negative deposition is observed. Scale bars, 1 μm.

after patterning by 30 keV ions. In this case, the ion fluence necessary to suppress nanoparticle adhesion on sample B is more than 1 order of magnitude higher than for 5 keV.

The data presented in Figure 2 demonstrate that both positive (Figure 2a) and negative (Figure 2d) deposition can be achieved by a proper choice of initial substrate termination and ion fluence. Additionally,

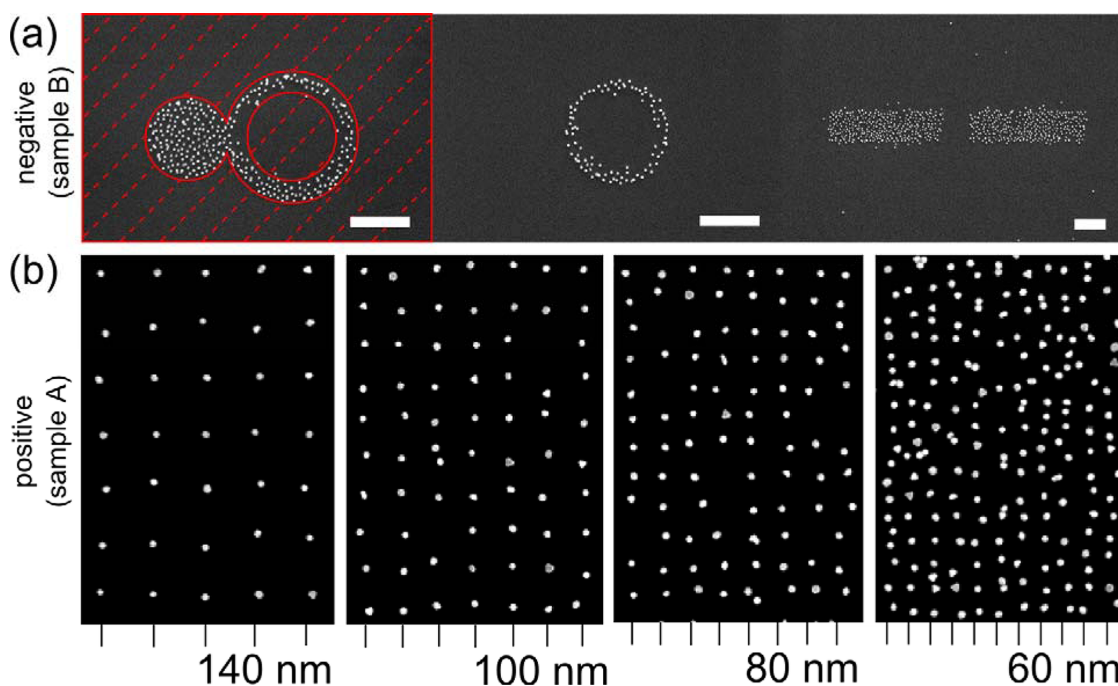

Figure 3. Demonstration of negative and positive deposition and precision placement tests. (a) Examples of negative deposition of 20 nm gold nanoparticles on sample B. After patterning by 5 keV Ga^+ ion beam with a high fluence (4×10^{15} cm^{-2}), the sample was immersed in the 3 mM HF-modified Au colloidal solution. The nanoparticles do not adhere to the areas irradiated by the ion beam (hatched in red). Scale bars, 500 nm. (b) Regular arrays of 20 nm gold nanoparticles on sample A patterned by the 30 keV ion beam (each spot exposed to the dose equivalent to ~2300 ions) and immersed into the 3 mM HF-modified Au colloidal solution (positive deposition). Ticks below the images mark the desired pattern periodicity, including the pitch.

altering the pH of the colloidal solution provides an alternative pathway for the positive/negative deposition on sample A. Such an experiment is shown in Figure 2h. Using the colloidal solution with a lower pH (12 mM HF-modified) and larger ion fluence (8×10^{14} cm^{-2}), an inverse deposition to that presented in Figure 2a on the same type of the sample is achieved.

The inspection of ion-beam-patterned areas carried out by Kelvin probe microscopy (KPM) before immersion of the samples into the colloidal solution revealed an increase in the contact potential difference (CPD) with the increasing ion fluence for both samples first (Figure 2f). Then, after reaching a certain maximum, the CPD starts to decrease with the ion fluence in case of sample B (Figure 2b,d, left, and Figure 2f). An identical measurement on sample A revealed only a dip in the CPD−ion fluence curve followed by a final increase to its maximal value at the highest fluences (Figure 2a,c, left, and Figure 2f). This behavior coincides with a pioneering work by Stevens-Kalceff and Kruss,[40] who also observed an overall CPD increase after irradiation by FIB up to certain ion fluences.

For low ion fluences, the measured CPD data correlate with the adhesion behavior of colloidal nanoparticles on both samples because, with the increasing local surface potential (being related to CPD),[41] the adhesion of negatively charged colloidal nanoparticles increases and thus their concentration on the sample grows. The decrease of the CPD with the ion fluence coincides with the decrease of nanoparticle concentration on sample B. However, in the case of sample A, the data of these two quantities do not correlate at higher ion fluences at all, as the nanoparticle adhesion is suppressed but the CPD gets even higher. This effect is most likely connected to the more profound contamination of surfaces at higher ion fluences.

In Figure 3a, an example of the negative selective deposition of 20 nm gold nanoparticles is presented. The nanoparticles adhere only to the areas not exposed to FIB (sample B, 5 keV Ga^+ beam, fluence 4×10^{15} cm^{-2}). In this way, the patterns of various shapes filled in with randomly arranged colloids have been achieved. However, the formation of sharp borders of these patterns turned out to be difficult. This uncertainty is caused by the low-intensity beam tail, resulting in undesired irradiation of the internal areas of the patterns adjacent to the borders (the effect being most visible in Figure 2c,h). This effect can be minimized by increasing the primary ion beam energy (which results in a narrower beam column at the surface and subsurface layers), but it has to be compensated by the application of higher ion fluences (as indicated in Figure 2e). The capability of the technique to create an array of regularly spaced 20 nm Au nanoparticles is demonstrated in Figure 3b. First, rectangular arrays of localized irradiated spots with different pitches (distance between the spots) were patterned on sample A by FIB. The sample

was immersed into the 3 mM HF-modified Au colloidal solution afterward. The most reliable and reproducible results of this positive selective deposition method were obtained for the pitch ≥120 nm and 30 keV Ga^+ beam. When the pitch is reduced, various proximity effects have been observed, mainly the adhesion of more nanoparticles per a single spot, decreasing placement precision, and loss of strict 2D periodicity. The low-intensity ion beam tail again plays a significant role since with the decreasing pitch the areas between the desired nanoparticle positions get more and more exposed to the ions. With the development of the focused ion beam technique, it is reasonable to expect the decrease of the pitch well below 100 nm. We also expect to achieve an improved placement precision using the focused electron beam.

DISCUSSION

The origin of the increase of the contact potential difference measured by KFM on areas irradiated by the ion beam is usually explained by the positive charging of subsurface layers due to ion implantation and secondary electron emission. It has been suggested that the charging can occur due to the formation of an amorphous zone below the ion beam impact site.[42−44] Such an amorphized region exhibits a decreased charge carrier mobility and concentration[44−46] due to the formation of defects acting as deep traps for charge carriers.[42,47] To test this hypothesis, we exposed the samples also to an electron beam. In this case, the amorphized zone is not formed and charge could be potentially stored only at the native oxide/silicon interface. However, we have observed behavior similar to the ion-beam-irradiated samples. For low fluences, the contact difference potential grows with the increasing fluence, then it decreases and becomes negative for very large fluences (see Figure S3 in Supporting Information). To investigate the role of an amorphous layer on charge trapping, similar experiments have been carried out on the samples covered by predeposited amorphous silicon films with different thicknesses (Figure S4 in Supporting Information). Although this film could potentially act as a charge storage layer,[48] these experiments show that the adhesion of nanoparticles does not depend on its thickness or the particle fluence and energy. Therefore, one can conclude that the charging caused by the charged particle beam does not play a major role here. The additional experiments show that the surface potential decay is extremely slow (Figure S5 in Supporting Information) and the CPD modification is detectable even a year after the exposure, which should not be the case of sample charging induced by the charged particle beam.

Taking into account the presented experiments, it is evident that the surface chemistry of the silicon substrate and especially of native oxide is a key issue to be addressed. Both ion and electron beams induce an increase in surface potential of the substrate for low fluences. Although the ion fluence is too low for noticeable sputtering of substrate atoms, it is sufficient to modify the atomic and molecular surface termination. In addition, the ion bombardment is likely to induce surface roughness and thus to increase the number of surface adsorption sites. The character of irradiated surface-terminating species is dependent on the pH of the colloidal solution. Although the hydrogen and methoxy termination on the surface of the pristine sample A is preserved in the 3 mM HF-modified solution, on the areas exposed to ions and electrons, it is replaced by −OH and $-OH_2^+$ termination, thus promoting adhesion of the nanoparticles. On the surface of sample B, the amount of positively charged terminating groups is increased for low fluences on the exposed areas, as well. The same results can be obtained using an electron beam.

For larger ion fluences, the surface is significantly damaged and the number of implanted Ga ions increases. However, no Ga has been detected by XPS (detection limit ∼0.1%) even after partial oxide removal by sample immersion in the 12 mM HF-modified solution (see Supporting Information, Figure S2). Hence, the isoelectric point of the silicon surface does not decrease due to the presence of Ga, but it is most probably caused by a different effect. Comparing the XPS spectra of the areas irradiated by low and large fluences, the major difference is a significant increase of adsorbates on the surface (mainly fluorine; see Figure S2), which is undoubtedly caused by the beam-assisted deposition (resulting from decomposition of adsorbed hydro- and fluorocarbons on the surface). We also note that fluorine and also carbon are known to increase hydrophobicity of the silicon surface.[49] Hence, the prevention of the deposition of colloidal nanoparticles can be attributed to the presence of a deposited contamination layer. The deposition induced by electron and ion beams becomes more effective with the decreasing primary beam energy,[50] due to the fact that the decomposition cross sections for many molecules, including hydro- and fluorocarbons, have a maximum for particle energy around 100 eV.[50,51] This statement holds for both ions and electrons and explains why the ion and electron fluences required for negative deposition increase with the primary beam energy (Figure 2e). Ions are, however, more efficient than electrons, especially at low fluences where the surface sputtering is negligible.

The proposed link between the surface termination and hydrophilic/hydrophobic properties of the surface explains also the nature of the CPD increase after beam irradiation. The increase of CPD with relative humidity was previously observed on SiO_2 substrates and attributed to the net positive charge or dipole formation on the surface with the increasing water layer thickness.[41] In our experiments, the hydrophilic −OH-terminated

areas (pristine sample B or low-fluence-exposed areas of samples A and B) show a CPD increase due to water adsorbed from ambient atmosphere, and in contrast, more hydrophobic −H- and $-CH_3$-terminated areas (sample A and high-fluence-exposed areas of samples A and B) show a CPD decrease. The nature of the CPD increase for fluences above 8×10^{14} cm^{-2} (Figure 2f) is still under debate and will be a subject of further investigation.

CONCLUSIONS

In summary, we have proved that the surface chemistry of the native silicon oxide modified by charged beams is responsible for the selective deposition of gold colloidal nanoparticles. By varying pH of the colloidal solution and fluence of the charged beam irradiating the sample surface, the control over adsorption of colloidal nanoparticles is achieved. Precise tuning of these parameters results in the deposition on both exposed or unexposed areas (positive or negative lithography, respectively). As an example of the positive deposition, we have demonstrated a simple maskless two-step process for the selective assembly of single gold nanoparticles with a 20 nm diameter with the pattern pitch parameter down to 140 nm onto silicon substrates covered with a native oxide layer. In the case of the negative deposition, random assemblies of gold nanoparticles within the patterns outlined by areas irradiated by a high-fluence charged particle beam were prepared. Even though the placement of a single isolated nanoparticle can be done with a precision of several nanometers, the existing proximity effects result in misplacing particles being part of arrays if the pitch smaller than 120 nm is used. These effects can be lowered using a better defined beam (preferentially electrons). Moreover, the exposure of patterned samples to ambient atmosphere could be replaced by an *in situ* exposure to specific gaseous precursors inside the microscope chamber. In this way, a better control over the adsorbed species and, thus potentially, the patterning resolution should be achieved.

Since no electret/resist layer has been involved in our approach, the presented method is suitable for fabrication of functional nanostructures where precise control over the position, concentration, and, additionally, nanoparticle/substrate interface is required. In this way, the gold catalyst for nanowire growth could be placed to a desired position directly on a Si substrate, as well as an array of gold nanoparticles for plasmonic applications, where the properties of substrate dielectric materials essentially affect their resonance frequencies.

METHODS

Wafer Fabrication Steps. Sample A (Siltronix, Si(111), resistivity 0.01 Ω·cm) was dried in hot isopropyl alcohol after the last SC1 bath, resulting in −H and $-CH_x$ termination of the native silicon oxide. In comparison with sample B, the presence of these surface groups increases the hydrophobicity of the surface. The last fabrication step in the case of sample B (ON semiconductor, Si(100), resistivity 6−9 Ω·cm) was rinsing in ultraclean water. Hence, the grown native oxide is −OH-terminated and hydrophilic. To exclude other possible explanations, we have also used Si(111) with a resistivity of 0.03 Ω·cm, treated in a similar way to sample B. Gold nanoparticle adhesion experiments have shown that the surface crystallographic orientation or doping level of the substrate does not play a significant role and that the surface termination is crucially dependent on the final fabrication step only.

Charged Particle Beam Patterning. The sample exposures were done using the FEI Helios Nanolab dual beam microscope. Each pixel of the test square patterns was exposed to the beam only once (single-loop scanning), and the beam overlap was set to a conventional value of 50%. The Ga^+ ion beam current was kept small (3.9 pA for 5 keV, 10 pA for 30 keV) to reduce the beam size to 20 and 10 nm, respectively, increasing thus the pattern resolution. The exposures were done at pressures below 2×10^{-4} Pa; this is crucial for minimizing beam spreading, especially for low-energy ion beams (<5 keV). The exposures to electron beams with energies below 1 keV were done in a retarding field arrangement by applying high voltage to the sample, resulting in reduced landing energy of electrons.

Nanoparticle Concentration Evaluation. To calculate the particle concentration on the surface, high-resolution SEM images were acquired on different parts of the samples. Each data point in Figure 2e was calculated from a sample area covered with several thousands of nanoparticles to get reasonable statistics.

Additional Experiments: XPS and KFM. Both XPS and KFM analyses of patterned samples were carried out within several minutes after removing the samples from the dual beam microscope. For the XPS analysis, the samples were introduced into an ultrahigh vacuum system equipped with a conventional X-ray source (Al Kα, 1486.6 eV) and hemispherical analyzer (both Omicron). To increase surface sensitivity, the electron exit angle was set to 11° with respect to the surface plane. The recorded peaks were fitted with the Voigt functions. The contact potential differences were measured by a SPM setup (NT-MDT) in the KFM mode using Au-covered silicon cantilevers (NSG 10 Au − NT-MDT) under ambient atmosphere conditions (relative humidity 45−55%) at room temperature (22 °C).

Conflict of Interest: The authors declare no competing financial interests.

Acknowledgment. The authors acknowledge J. Stuchlík from the Institute of Physics ASCR for deposition of amorphous Si layers, F. Münz from Masaryk University for the assistance with FTIR measurements, A. Bábík from Faculty of Chemistry BUT for performing the wetting angle measurements, and J. Čechal for discussions on XPS spectra interpretation. This work was supported by the Grant Agency of the Czech Republic (P108/12/P699), European Regional Development Fund (CEITEC, CZ.1.05/1.1.00/02.0068) and by the EU seventh Framework Programme under the "Capacities" specific programme (Contract No. 286154, SYLICA). M. K. acknowledges the support of FEI Company.

Supporting Information Available: Supporting Figures S1 and S2 showing XPS, FTIR, and wetting angle measurements, and Supporting Figures S3, S4, and S5 with additional experiments on nanoparticle adhesion. This material is available free of charge *via* the Internet at http://pubs.acs.org.

REFERENCES AND NOTES

1. Manandhar, P.; Akhadov, E. A.; Tracy, C.; Picraux, S. T. Integration of Nanowire Devices in Out-of-Plane Geometry. *Nano Lett.* **2010**, *10*, 2126–2132.

2. Schmid, H.; Bessire, C.; Björk, M. T.; Schenk, A.; Riel, H. Silicon Nanowire Esaki Diodes. *Nano Lett.* **2012**, *12*, 699–703.
3. Sutter, E.; Sutter, P. Phase Diagram of Nanoscale Alloy Particles Used for Vapor−Liquid−Solid Growth of Semiconductor. *Nano Lett.* **2008**, *8*, 411–414.
4. Huang, Z.; Geyer, N.; Werner, P.; de Boor, J.; Gösele, U. Metal-Assisted Chemical Etching of Silicon: A Review. *Adv. Mater.* **2010**, *23*, 285–308.
5. Oh, Y.; Choi, C.; Hong, D.; Kong, S. D.; Jin, S. Magnetically Guided Nano-Micro Shaping and Slicing of Silicon. *Nano Lett.* **2012**, *12*, 2045–2050.
6. Halas, N. J.; Lal, S.; Chang, W.-S.; Link, S.; Nordlander, P. Plasmons in Strongly Coupled Metallic Nanostructures. *Chem. Rev.* **2011**, *111*, 3913–3961.
7. Wei, Q.-H.; Su, K.-H.; Durant, S.; Zhang, X. Plasmon Resonance of Finite One-Dimensional Au Nanoparticle Chains. *Nano Lett.* **2004**, *4*, 1067–1071.
8. Krenn, J. R.; Salerno, N.; Felidj, N.; Lamprecht, B.; Schider, G.; Leitner, A.; Aussenegg, F. R.; Weeber, J. C.; Dereux, A.; Goudonnet, J. P. Light Field Propagation by Metal Micro-and Nanostructures. *J. Microsc.* **2001**, *202*, 122–128.
9. Lal, S.; Link, S.; Halas, N. Nano-optics from Sensing to Waveguiding. *Nat. Photonics* **2007**, *1*, 641–648.
10. Albaladejo, S.; Sáenz, J. J.; Marqués, M. I. Plasmonic Nanoparticle Chain in a Light Field: A Resonant Optical Sail. *Nano Lett.* **2011**, *11*, 4597–4600.
11. Morag, A.; Philosof-Mazor, L.; Volinsky, R.; Mentovich, E.; Richter, S.; Jelinek, R. Self-Assembled Transparent Conductive Electrodes from Au Nanoparticles in Surfactant Monolayer Templates. *Adv. Mater.* **2011**, *23*, 4327–4331.
12. Lin, H.-Y.; Tsai, L.-C.; Chen, C.-H. Assembly of Nanoparticle Patterns with Single-Particle Resolution Using DNA-Mediated Charge Trapping Technique: Method and Applications. *Adv. Funct. Mater.* **2007**, *17*, 3182–3186.
13. Kramer, R. K.; Pholchai, N.; Sorger, V. J.; Yim, T. J.; Oulton, R.; Zhang, X. Positioning of Quantum Dots on Metallic Nanostructures. *Nanotechnology* **2010**, *21*, 145307.
14. Städler, B.; Solak, H. H.; Frerker, S.; Bonroy, K.; Frederix, F.; Vörös, J.; Grandin, H. M. Nanopatterning of Gold Colloids for Label-Free Biosensing. *Nanotechnology* **2007**, *18*, 155306.
15. Lalander, C.; Zheng, Y.; Dhuey, S.; Cabrini, S.; Bach, U. DNA-Directed Self-Assembly of Gold Nanoparticles onto Nanopatterned Surfaces: Controlled Placement into Regular Arrays. *ACS Nano* **2010**, *4*, 6153–6161.
16. Coskun, U. C.; Mebrahtu, H.; Huang, P. B.; Huang, J.; Sebba, D.; Biasco, A.; Makarovski, A.; Lazarides, A.; LaBean, T. H.; Finkelstein, G. Single-Electron Transistors Made by Chemical Patterning of Silicon Dioxide Substrates and Selective Deposition of Gold Nanoparticles. *Appl. Phys. Lett.* **2008**, *93*, 123101.
17. Jiang, L.; Wang, W.; Fuchs, H.; Chi, L. One-Dimensional Arrangement of Gold Nanoparticles with Tunable Interparticle Distance. *Small* **2009**, *5*, 2819–2822.
18. Gilles, S.; Kaulen, C.; Pabst, M.; Simon, U.; Offenhäusser, A.; Mayer, D. Patterned Self-Assembly of Gold Nanoparticles on Chemical Templates Fabricated by Soft UV Nanoimprint Lithography. *Nanotechnology* **2011**, *22*, 295301.
19. Ma, L.-C.; Subramanian, R.; Huang, H.-W.; Ray, V.; Kim, C.-U.; Koh, S. J. Electrostatic Funneling for Precise Nanoparticle Placement: A Route to Wafer-Scale Integration. *Nano Lett.* **2007**, *7*, 439–445.
20. Fustin, C.-A.; Glasser, G.; Spiess, H. W.; Jonas, U. Parameters Influencing the Templated Growth of Colloidal Crystals on Chemically Patterned Surfaces. *Langmuir* **2004**, *20*, 9114–9123.
21. Nidetz, R.; Kim, J. Directed Self-Assembly of Nanogold Using a Chemically Modified Nanopatterned Surface. *Nanotechnology* **2012**, *23*, 045602.
22. Jiang, L.; Sun, Y.; Nowak, C.; Kibrom, A.; Zou, C.; Ma, J.; Fuchs, H.; Li, S.; Chi, L.; Chen, X. Patterning of Plasmonic Nanoparticles into Multiplexed One-Dimensional Arrays Based on Spatially Modulated Electrostatic Potential. *ACS Nano* **2011**, *5*, 8288–8294.
23. Tzeng, S.-D.; Lin, K.-J.; Hu, J.-C.; Chen, L.-J.; Gwo, S. Templated Self-Assembly of Colloidal Nanoparticles Controlled by Electrostatic Nanopatterning on a Si_3N_4/SiO_2/Si Electret. *Adv. Mater.* **2006**, *18*, 1147–1151.
24. Barry, C. R.; Gu, J.; Jacobs, H. O. Charging Process and Coulomb-Force-Directed Printing of Nanoparticles with Sub-100-nm Lateral Resolution. *Nano Lett.* **2005**, *5*, 2078–2084.
25. Ressier, L.; Palleau, E.; Garcia, C.; Viau, G.; Viallet, B. How To Control AFM Nanoxerography for the Templated Monolayered Assembly of 2 nm Colloidal Gold Nanoparticles. *IEEE Trans. Nanotechnol.* **2009**, *8*, 487–491.
26. Palleau, E.; Sangeetha, N. M.; Viau, G.; Marty, J.-D.; Ressier, L. Coulomb Force Directed Single and Binary Assembly of Nanoparticles from Aqueous Dispersions by AFM Nanoxerography. *ACS Nano* **2011**, *5*, 4228–4235.
27. Onses, M. S.; Pathak, P.; Liu, C.-C.; Cerrina, F.; Nealey, P. F. Localization of Multiple DNA Sequences on Nanopatterns. *ACS Nano* **2011**, *5*, 7899–7909.
28. Mikkelsen, A.; Eriksson, J.; Lundgren, E.; Andersen, J. N.; Weissenreider, J.; Seifert, W. The Influence of Lysine on InP(001) Surface Ordering and Nanowire Growth. *Nanotechnology* **2005**, *16*, 2354–2359.
29. Novotny, L.; Hecht, J. *Principles of Nano-optics*; Cambridge University Press: New York, 2006; pp 403−406.
30. Torchinsky, I.; Amdursky, N.; Inberg, A.; Rosenman, G. Electron-Induced Adhesion and Patterning of Gold Nanoparticles. *Appl. Phys. Lett.* **2010**, *96*, 093106.
31. Fudouzi, H.; Kobayashi, M.; Shinya, N. Site-Controlled Deposition of Microsized Particles Using an Electrostatic Assembly. *Adv. Mater.* **2002**, *14*, 1649–1652.
32. Fudouzi, H.; Kobayashi, M.; Shinya, N. Assembling 100nm Scale Particles by an Electrostatic Potential Field. *J. Nanopart. Res.* **2001**, *3*, 193–200.
33. Shahmoon, A.; Limon, O.; Girshevitz, O.; Fleger, Y.; Demir, H. V.; Zalevsky, Z. Tunable Nano Devices Fabricated by Controlled Deposition of Gold Nanoparticles *via* Focused Ion Beam. *Microelectron. Eng.* **2010**, *87*, 1363–1366.
34. Busnanina, A.; Park, J.-G.; Bakhtari, K. Particle Deposition and Adhesion. In *Handbook of Silicon Wafer Cleaning Technology*, 2nd ed.; Reinhardt, K. A.; Kern, W., Eds.; William Andrew Inc: Norwich, NY, 2008; p 186.
35. Guhathakurta, S.; Subramanian, A. Effect of Hydrofluoric Acid in Oxidizing Acid Mixtures on the Hydroxylation of Silicon Surface. *J. Electrochem. Soc.* **2007**, *154*, P136.
36. Pokrovsky, O. S.; Golubev, S. V.; Mielczarski, J. A. Kinetic Evidences of the Existence of Positively Charged Species at the Quartz−Aqueous Solution Interface. *J. Colloid Interface Sci.* **2006**, *296*, 189–194.
37. Duval, Y.; Mielczarski, J. A.; Pokrovsky, O. S.; Mielczarski, E.; Ehrhardt, J. J. Evidence of the Existence of Three Types of Species at the Quartz−Aqueous Solution Interface at pH 0−10: XPS Surface Group Quantification and Surface Complexation Modeling. *J. Phys. Chem. B* **2002**, *106*, 2937–2945.
38. Morita, M.; Ohmi, T.; Hasegawa, E.; Kawakami, M.; Ohwada, M. Growth of Native Oxide on a Silicon Surface. *J. Appl. Phys.* **1990**, *68*, 1272–1280.
39. Ward, J. W.; Kubena, R. L.; Utlaut, M. W. Transverse Thermal Velocity Broadening of Focused Beams from Liquid Metal Ion Sources. *J. Vac. Sci. Technol., B* **1988**, *6*, 2090–2094.
40. Stevens-Kalceff, M. A.; Kruss, D. P. Focused Ion Beam Induced Local Modifications of the Contact Potential Difference of n- and p-Doped Silicon. *J. Phys. D: Appl. Phys.* **2009**, *42*, 145117.
41. Verdaguer, A.; Weis, C.; Oncins, G.; Ketteler, G.; Bluhm, H.; Salmeron, M. Growth and Structure of Water on SiO_2 Films on Si Investigated by Kelvin Probe Microscopy and *In Situ* X-ray Spectroscopies. *Langmuir* **2007**, *23*, 9699–9703.
42. Hopf, T.; Yang, C.; Andersen, S. E.; Jamieson, D. N. The Response of Silicon Detectors to Low-Energy Ion Implantation. *J. Phys.: Condens. Matter* **2008**, *20*, 415205.
43. Moberly Chan, W. J.; Adams, D. P.; Aziz, M. J.; Hobler, G.; Schenkel, T. Fundamentals of Focused Ion Beam Nanostructural Processing: Below, At, and Above the Surface. *MRS Bull.* **2007**, *32*, 424–432.

44. Lugstein, A.; Brezna, W.; Hobler, G.; Bertagnolli, E. Method To Characterize the Three-Dimensional Distribution of Focused Ion Beam Induced Damage in Silicon After 50 keV Ga^+ Irradiation. *J. Vac. Sci. Technol., A* **2003**, *21*, 1644–1648.
45. Spoldi, G.; Beuer, S.; Rommel, M.; Yanev, V.; Bauer, A. J.; Ryssel, H. Experimental Observation of FIB Induced Lateral Damage on Silicon Samples. *Microelecron. Eng.* **2009**, *86*, 548–551.
46. Rommel, M.; Spoldi, G.; Yanev, V.; Beuer, S.; Amon, B.; Jambreck, J.; Petersen, S.; Bauer, A. J. Comprehensive Study of Focused Ion Beam Induced Lateral Damage in Silicon by Scanning Probe Microscopy Studies. *J. Vac. Sci. Technol., B* **2010**, *28*, 595–607.
47. Palko, J. W.; Srour, J. R. Amorphous Inclusions in Irradiated Silicon and Their Effects on Material and Device Properties. *IEEE Trans. Nucl. Sci.* **2008**, *55*, 2992–2999.
48. Rezek, B.; Mates, T.; Stuchlík, J.; Kočka, J.; Stemmer, A. Charge Storage in Undoped Hydrogenated Amorphous Silicon by Ambient Atomic Force Microscopy. *Appl. Phys. Lett.* **2003**, *83*, 1764–1766.
49. Zhang, X. G. *Electrochemistry of Silicon and Its Oxide*; Kluwer Academic Publishers: New York, 2001; pp 70−71.
50. Botman, A.; de Winter, D. A. M.; Mulders, J. J. L. Electron-Beam-Induced Deposition of Platinum at Low Landing Energies. *J. Vac. Sci. Technol., B* **2008**, *26*, 2460–2463.
51. Utke, I.; Hoffmann, P.; Melngailis, J. Gas-Assisted Focused Electron Beam and Ion Beam Processing and Fabrication. *J. Vac. Sci. Technol., B* **2008**, *26*, 1197–1276.